



# Tomography of the Solar Corona with the *Metis* Coronagraph I: Predictive Simulations with Visible-Light Images

Alberto M. Vásquez<sup>1,2</sup> · Federico A. Nuevo<sup>1,3</sup> · Federica Frassati<sup>4</sup> ·  
Alessandro Bemporad<sup>4</sup> · Richard A. Frazin<sup>5</sup> · Marco Romoli<sup>6</sup> ·  
Nishtha Sachdeva<sup>5</sup> · Ward B. Manchester IV<sup>5</sup>

Received: 8 September 2021 / Accepted: 31 July 2022  
© The Author(s), under exclusive licence to Springer Nature B.V. 2022

## Abstract

The *Solar Orbiter/Metis* coronagraph records full-Sun visible-light polarized brightness (*pB*-) images of the solar corona. This work investigates the utility of a synoptic observational program of *Metis* for tomographic reconstruction of the three-dimensional (3D) distribution of the electron density of the global solar corona. During its lifetime, the mission's distance to the Sun will range over  $\approx 0.3 - 1.0$  AU, while its solar latitude will span  $\approx \pm 33^\circ$ . The limitations that this orbital complexity poses on tomographic reconstructions are explored in this work. Using the predicted orbital information of *Solar Orbiter* and 3D-MHD simulations of the solar corona using the Alfvén Wave Solar atmosphere Model (AW-SoM), time series of synthetic *Metis pB*-images were computed and used as data to attempt tomographic reconstruction of the model. These numerical experiments were implemented for solar-minimum and solar-maximum conditions. In both cases, images were synthesized from three orbital segments, corresponding to extreme geometrical conditions of observation by *Metis*: aphelion, perihelion, and maximum solar latitude. The range of heights that can be reconstructed, the required data-gathering period, and the accuracy of the reconstruction, are discussed in detail for each case. As a general conclusion, a *Metis* synoptic observational program with a cadence of at least four images day<sup>-1</sup> provides enough data to attempt tomographic reconstructions during the whole lifetime of the mission, a requirement well within the two- to three-hour cadence of the current synoptic program. This program will allow implementation of tomography experimenting with different values for the cadence of the time series of images used to feed reconstructions. Its cadence will also provide continuous opportunities to select images avoiding highly dynamic events, which compromise the accuracy of tomographic reconstructions.

**Keywords** Spectrum, Visible · Corona, Structures · Corona, Models · Solar Cycle

## 1. Introduction

One of the most direct diagnostics of the electron density of the solar corona is provided by its free electrons' Thomson scattering the intense photospheric visible-light (VL) radiation (Minnaert, 1930). Methods to determine the three-dimensional (3D) structure of the electron

---

Extended author information available on the last page of the article

density of the corona based on VL-images date back to the pioneering work by van de Hulst (1950), which used eclipse images assuming azimuthal symmetry. Since then, methods have evolved into modern solar rotational tomography (SRT) techniques, which make no use of ad-hoc modeling of the coronal structure. Methods include static-SRT (Frazin, 2000; Frazin and Janzen, 2002), which assumes a static corona, as well as time-dependent ones based on different approaches such as Kalman filtering (Butala et al., 2010) and temporal regularization (Vibert et al., 2016; Barbey, Guennou, and Auchère, 2013). Extensive reviews on the development of SRT, as well as its technical details, can be found in those works and references therein.

SRT currently constitutes the only observational technique capable of providing an empirical model-free 3D description of the coronal structure at a global scale. As such, it is of great relevance to the continued development and validation of state-of-the-art 3D magnetohydrodynamical (MHD) models of the solar corona and solar wind (Vázquez, 2016; Lloveras et al., 2020).

Existing SRT studies using VL-images are based on data provided by (either ground-based or space-borne) coronagraphs in  $\approx 1$  AU circular orbits around the Sun. With the new generation of solar observatories in highly eccentric orbits carrying VL-telescopes, namely the *Parker Solar Probe* (PSP) and the *Solar Orbiter* (Müller et al., 2020; García Marirrodriga et al., 2021) missions, new opportunities arise for development and application of tomographic techniques. Vázquez et al. (2019) recently investigated the use of images provided by the PSP/*Wide-field Imager* (WISPR) instrument to carry out tomography of the solar corona.

The *Solar Orbiter/Metis* coronagraph (Antonucci et al., 2020) records both ultraviolet Lyman- $\alpha$  and VL polarized brightness ( $pB$ ) full-Sun images of the solar corona. Independently of the main observational time intervals of *Metis* (Antonucci et al., 2020), specific orbital segments over which it will observe in full resolution and high cadence, a continuous synoptic observational program will be implemented. This work explores the utility of such a program in terms of using its  $pB$ -images for tomographic reconstruction of the 3D-distribution of the electron density of the global solar corona.

This study is motivated by the highly eccentric orbit of *Solar Orbiter* and its changing latitudinal vantage point. The changing *Solar Orbiter*–Sun distance [ $D$ ] implies that the radial field of view (FoV) of *Metis* will continuously vary, and so will the range of heights that can be reconstructed. The changing orbital speed of the spacecraft implies that the time required to observe the corona from enough view angles to constrain the tomographic inversion problem will also vary with time. The changing latitude [ $\theta$ ] of the vantage point of *Metis* also imposes restrictions, as with increasing latitude the lines-of-sight (LOS) associated with the images miss an increasing fraction of the volume of the solar corona.

This work applies the strategy of Vázquez et al. (2019), which explored the use of PSP/WISPR images for tomography. Using the predicted orbital information of *Solar Orbiter* and the specifications of the *Metis* instrument, synthetic  $pB$ -images were computed based on 3D-MHD simulations of the solar corona. The data were then used to attempt tomographic reconstructions of the models. As this study focuses on assessing what is the impact of the complex geometry of the *Metis* observations in tomographic reconstructions, steady-state simulations were used in order to not introduce dynamics-induced artifacts. In order to assess how the different geometric aspects of the observations constrain the capacity of carrying out tomography, images were synthesized from three orbital locations corresponding to extreme geometrical conditions of observation by *Metis*. To investigate the quality of the reconstructions upon coronal complexity, the three numerical experiments were implemented for two Carrington rotations (CRs), selected from a solar minimum and a solar maximum, respectively.

## 2. Methodology

### 2.1. 3D-MHD Model of the Solar Corona

The Alfvén Wave Solar atmosphere Model (AWSoM: Sokolov et al. 2013, van der Holst et al. 2014), within the Space-Weather Modeling Framework (SWMF), was used in this work to simulate the solar corona. The input data that drive the AWSoM model are from a single synoptic magnetogram, used to set the radial component of the magnetic field [ $B_r$ ] and the Alfvén-wave energy flux at the inner boundary, which corresponds to the upper chromosphere. For the simulations of this work, maps from the *Global Oscillation Network Group* (GONG) were used, with application of the Air Force Data Assimilation Photospheric Flux Transport model (ADAPT: Arge et al. 2013). The ADAPT-GONG maps provide a physics-based description of the unobserved polar magnetic fields by incorporating large-scale flux-transport processes including differential rotation, meridional flows, and supergranular flows.

Steady-state AWSoM simulations were run based on ADAPT-GONG maps for two different time periods. To experiment on the simplest possible coronal configuration, CR 2082 (05 April through 03 May 2009) was selected from the Solar Cycle (SC) 23/24 minimum, when the corona exhibited a strong azimuth symmetry, with an equatorial streamer belt dominating low latitudes and coronal holes (CHs) confined to high latitudes in both hemispheres (Lloveras et al., 2020). To study a highly complex coronal configuration, CR 2152 (28 June 28 through 25 July 2014) was selected during the peak of SC 24, when the corona showed both streamers and CHs at all latitudes (Sachdeva et al., 2021). The AWSoM model uses an adaptive-mesh-refinement scheme. Over the range of heliocentric height  $1 - 12 R_{\odot}$  the model was interpolated onto a uniform spherical grid with a resolution of  $\Delta r = 0.05 R_{\odot}$  in the radial direction, and  $\Delta\theta = \Delta\phi = 1^\circ$  in both latitude and longitude, finer than the resolution of the tomographic grid (detailed in Section 2.4).

### 2.2. The *Solar Orbiter* Orbit and Selected Segments

Three segments of the *Solar Orbiter* orbit were selected for simulation. Figure 1 shows plots of the temporal evolution of orbital parameters of the *Solar Orbiter* mission for its full lifetime. The top panel is a plot of the *Solar Orbiter*–Sun distance [ $D$ ], while the bottom panel shows the solar latitude [ $\theta$ ] of *Solar Orbiter*. The three red dots highlight the orbital locations around which simulations were implemented: an aphelion ( $D \approx 0.95$  AU) and a perihelion ( $D \approx 0.29$  AU) location, both during 2023, and a location of maximum solar latitude ( $\theta \approx +33^\circ$ ) during 2029.

For the three simulated observation sequences, Figure 2 shows the radial FoV of *Metis* as a function of time (left panels), as well as the solar latitude of *Solar Orbiter* (right panels). From top to bottom, the panels show the simulations for the aphelion, the perihelion, and the maximum solar latitude locations, respectively. In these examples, the step of the solar longitude of *Solar Orbiter* between consecutive observations is set to  $\Delta\phi = 12^\circ$ . In this way, 16 observations span a total of  $\Delta\phi = 180^\circ$ , allowing off-limb observations of all coronal longitudes. In each left panel, the two horizontal dashed lines indicate the limits of the radial FoV that is common to all the images in the full sequence. Within this range of heights, data are then provided by the time series from all of its viewing angles.

The locations selected to simulate the image sequences complement each other, representing the different extreme geometrical conditions of observation along the *Solar Orbiter* orbit. Around the aphelion ( $D \approx 0.95$  AU), all images provide approximately the same radial

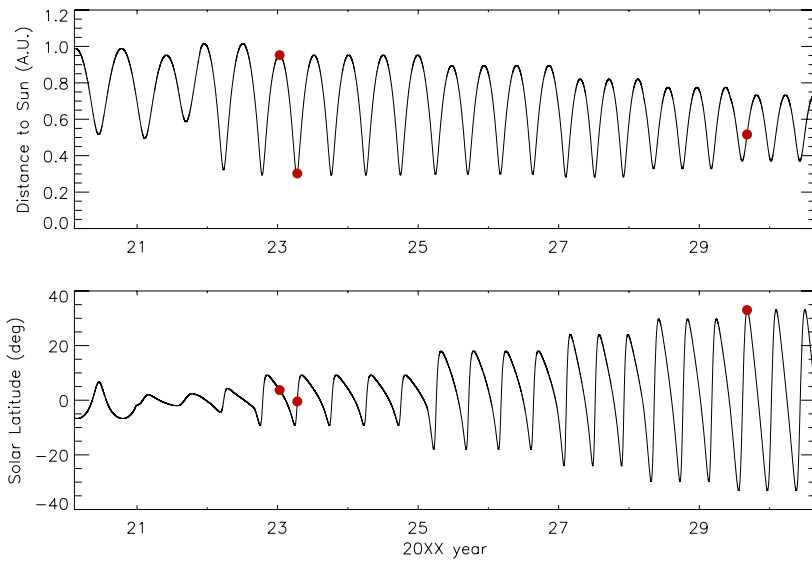


**Figure 1** *Solar Orbiter* orbit. *Top panel*: temporal evolution of the *Solar Orbiter*–Sun distance. *Bottom panel*: temporal evolution of the solar latitude of the disk center as seen by *Metis*. The *three red dots* highlight orbital points centered around which data acquisition is simulated in this work: an aphelion and a perihelion (during 2023), and a location for which *Solar Orbiter*’s latitude reaches a maximum value (during 2029).

$\text{FoV} \approx 5.7 - 10.3 R_{\odot}$ . For this first sequence the latitude vantage point is nearly constant and very close to the Equator, ranging  $\approx +3.0^{\circ}$  to  $+4.5^{\circ}$ . Around the selected perihelion ( $D \approx 0.29$  AU), the radial FoV changes non-monotonically with the *Solar Orbiter*–Sun distance, with the full sequence common FoV being  $\approx 2.3 - 3.2 R_{\odot}$ . For this second sequence, the latitude of the vantage point increases monotonically, ranging  $\approx -9.0^{\circ}$  to  $+7.0^{\circ}$ , still exploring low latitudes. Around the maximum latitude location ( $D \approx 0.5$  AU), the radial FoV increases monotonically, being the FoV common to all images  $\approx 3.5 - 5.0 R_{\odot}$ . For this third sequence, the latitude is nearly constant, ranging  $\approx +30^{\circ}$  to  $+33^{\circ}$ , reaching the maximum latitude to be explored by *Solar Orbiter*. Depending on the *Solar Orbiter*–Sun distance, the data-gathering periods of the sequences taken around the aphelion, perihelion, and maximum latitude locations are  $\approx 13, 22,$  and  $16$  days, respectively.

### 2.3. *Metis* Synthetic Images

Based on the two AWOSoM simulations described in Section 2.1, time series of synthetic *Metis* *pB*-images of the solar corona were computed for the three orbital segments detailed in Section 2.2. The images were computed by means of line-of-sight (LOS) integrals of the 3D-distribution of the electron density of a model of the solar corona times the appropriate Thomson-scattering weighting factor (Minnaert, 1930; van de Hulst, 1950). To compute the intensity of every pixel in the synthetic images, the implementation of the LOS integral makes use of the same numerical algorithm used by the tomographic inversion (described in Section 2.4). This is important for consistency between the forward problem (computation of images from the model) and the inverse one.

For the aphelion sequence, the first, middle, and last images are shown in the left, middle, and right panels of Figure 3, respectively. The top images (which indicate the relevant

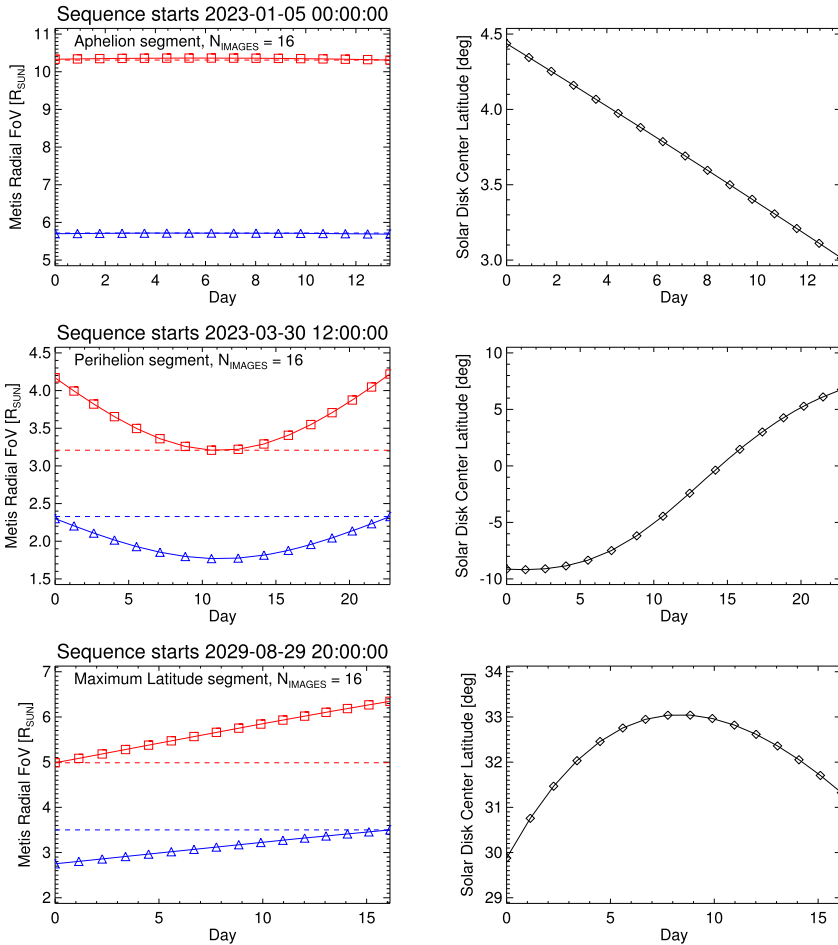


**Figure 2** Temporal evolution of the *Metis* radial FoV (left panels), and *Solar Orbiter*'s solar latitude (right panels), for the three time series of simulated observations. The top, middle, and bottom panels show the series around the aphelion, perihelion, and maximum-latitude locations, respectively. In each series, *Solar Orbiter*'s solar longitude  $\phi$  varies by  $\Delta\phi = 12^\circ$  between consecutive observations. In the left panels, for each observing date, the *Metis* radial FoV extends from the inner radius, indicated by the blue triangle, up to the outer radius, indicated by the red square. The horizontal dashed lines indicate the inner and outer limits of the radial FoV that is common to all the images in the full sequence.

ephemeris) correspond to the CR 2082 solar-minimum simulation, while the bottom ones correspond to the CR 2152 solar-maximum simulation. In each image, the two white rings indicate projected heliocentric heights  $5.7$  and  $10.3 R_{\odot}$ , the boundaries of the radial FoV common to all the images in the sequence. As for this sequence, the *Solar Orbiter*–Sun distance is roughly constant, so is the radial FoV. Also for this sequence the solar latitude of *Solar Orbiter* is nearly constant and very close to the Equator. As a result, the points of view of *Metis* for the first and last images of the sequence are nearly opposite, so that the resulting images are nearly East/West mirror images of each other, for both the CR 2082 and CR 2152 simulations.

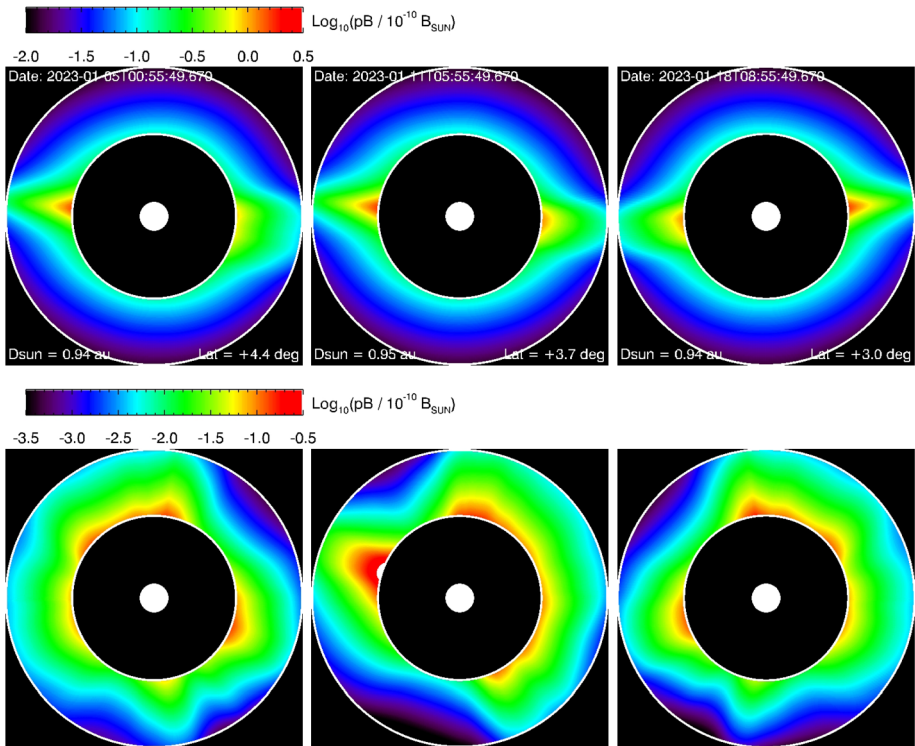


**Figure 3** Synthetic *Metis* *pB*-images for the aphelion segment, computed from the CR 2082 solar-minimum simulation (*top panels*) and the CR 2152 solar-maximum simulation (*bottom panels*). From *left to right* the images correspond to the first, middle, and last data point of the sequence shown in the top panel of Figure 2, with the top panels presenting the observation date and the distance to the Sun and solar latitude of *Solar Orbiter*. In each image, the *black circle* represents the inner occulter and the *white disk* the occulted solar disk. The *two white rings* indicate the boundaries of the radial FoV common to all the images in the sequence, at projected heliocentric heights  $5.7$  and  $10.3 R_{\odot}$ . For this series, the *Solar Orbiter*–Sun distance ranges  $\approx 0.94 - 0.95$  AU, while *Solar Orbiter*’s solar latitude ranges  $\approx +4.4^{\circ}$  to  $+3.0^{\circ}$ . Note the roughly constant size of the solar disk.

For the perihelion sequence, the first, middle, and last images are shown in the left, middle, and right panels of Figure 4, respectively. The top images correspond to the CR 2082 solar-minimum simulation, while the bottom ones correspond to the CR 2152 solar-maximum simulation. In each image, the two white rings indicate projected heliocentric heights  $2.3$  and  $3.2 R_{\odot}$ , the boundaries of the radial FoV common to all the images in the sequence. In this sequence the *Solar Orbiter*–Sun distance varies in the range  $\approx 0.38 - 0.29$  AU. The inner limit of the common radial FoV ( $\approx 2.3 R_{\odot}$ ) is imposed by the more distant images (first and last ones), while the outer limit of the common radial FoV ( $\approx 3.2 R_{\odot}$ ) is imposed by the perihelion (middle) image. *Solar Orbiter*’s excursion in solar latitude for this series, which is wider than in the aphelion case, is still limited to rather low latitudes. As the series is centered around perihelion, the first and last images are simulated from the same distance to the Sun. As a result, the first and last images are again nearly East/West mirror images of each other, for both the CR 2082 and CR 2152 simulations.

For the maximum-solar-latitude sequence, the first, middle, and last images are shown in the left, middle, and right panels of Figure 5, respectively. The top images correspond

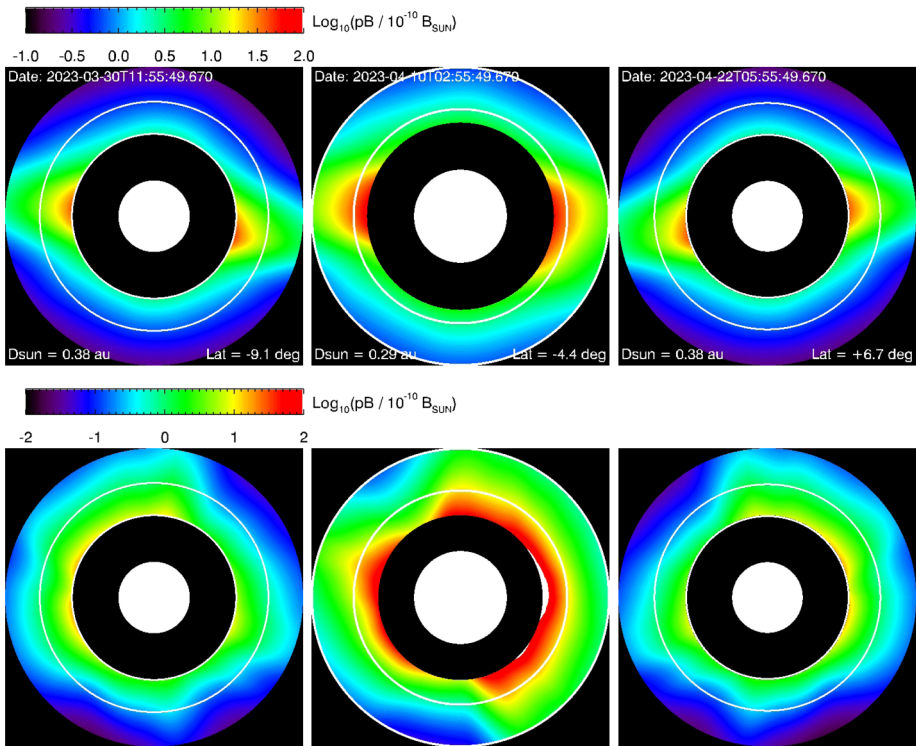


**Figure 4** Synthetic *Metis* *pB*-images for the perihelion segment, computed from the CR 2082 solar-minimum simulation (*top panels*) and the CR 2152 solar-maximum simulation (*bottom panels*). From *left to right* the images correspond to the first, middle, and last data point of the sequence shown in the middle panel of Figure 2, with the top panels presenting the observation date and the distance to the Sun and solar latitude of *Solar Orbiter*. In each image, the *black circle* represents the inner occulter and the *white disk* the occulted solar disk. The *two white rings* indicate the boundaries of the radial FoV common to all the images in the sequence, at projected heliocentric heights  $2.3$  and  $3.2 R_{\odot}$ . For this series, the *Solar Orbiter*–Sun distance ranges  $\approx 0.38 - 0.29$  AU, while *Solar Orbiter*'s solar latitude ranges  $\approx -9.1^{\circ}$  to  $+6.7^{\circ}$ . Note the larger size of the solar disk at perihelion (*middle panels*).

to the CR 2082 solar-minimum simulation, while the bottom ones correspond to the CR 2152 solar-maximum simulation. In each image, the two white rings indicate projected heliocentric heights  $3.5$  and  $5.0 R_{\odot}$ , the boundaries of the radial FoV common to all the images in the sequence. In this sequence the *Solar Orbiter*–Sun distance varies in the range  $\approx 0.45 - 0.58$  AU. The outer limit of the common radial FoV ( $\approx 5.0 R_{\odot}$ ) is imposed by the less distant observation (first one), while the outer limit of the common radial FoV ( $\approx 3.5 R_{\odot}$ ) is imposed by the more distant observation (last one). For this series, *Solar Orbiter*'s solar latitude is nearly constant and quite large, so that streamer structures are not observed edge-on as in the previous two cases. As a result, these images exhibit less prominent and wider streamers, and they are characterized by a smaller dynamic range.

## 2.4. SRT, Computational Grid, and Image Size

SRT uses a time series of coronal images (taken at a wavelength for which the corona is optically thin) to pose a linear inversion problem. The combination of the solar rotation and

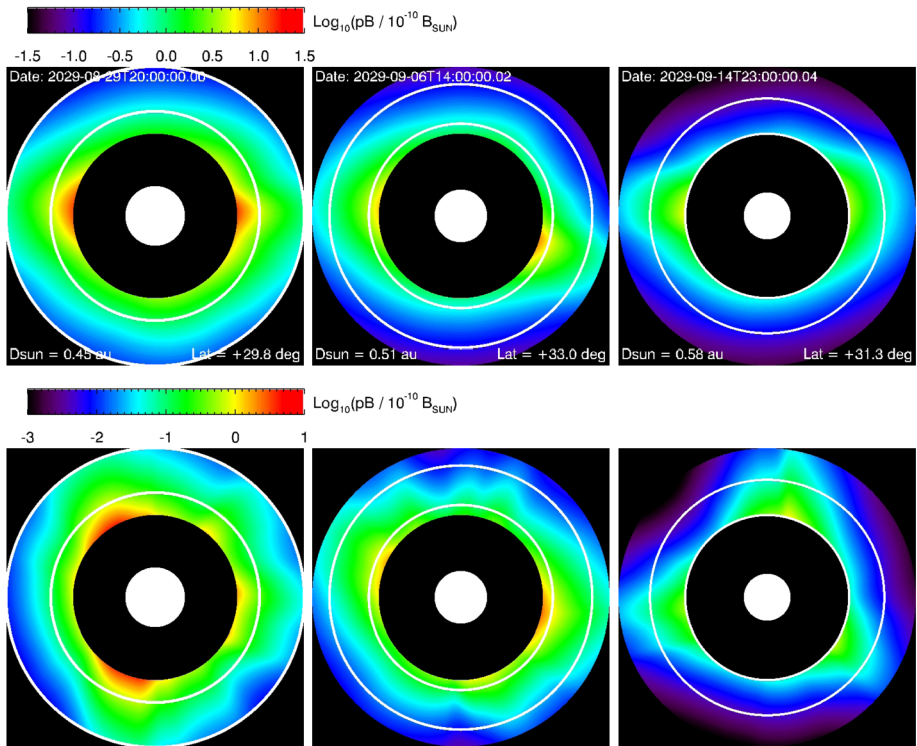


**Figure 5** Synthetic *Metis*  $pB$ -images for the maximum-latitude segment, computed from the CR 2082 solar-minimum simulation (*top panels*) and the CR 2152 solar-maximum simulation (*bottom panels*). From *left to right* the images correspond to the first, middle, and last data point of the sequence shown in the bottom panel of Figure 2, with the top panels presenting the observation date and the distance to the Sun and solar latitude of *Solar Orbiter*. In each image, the *black circle* represents the inner occulter and the *white disk* the occulted solar disk. The *two white rings* indicate the boundaries of the radial FoV common to all the images in the sequence, at projected heliocentric heights  $3.5$  and  $5.0 R_{\odot}$ . For this series, the *Solar Orbiter*–Sun distance ranges  $\approx 0.45 - 0.58$  AU, while *Solar Orbiter*'s solar latitude ranges  $\approx +29.8^{\circ}$  to  $+33.0^{\circ}$ . Note the decreasing size of the solar disk with increasing distance.

the orbital motion of the observer provide the required view angles. Each image in the series is a 2D projection of an underlying 3D emissivity structure. The intensity registered by a single pixel is the result of a LOS integral of the coronal emissivity. In the case of VL  $pB$ -images, this emissivity is proportional to the coronal electron density times a known geometrical factor. The intensity values of each pixel of every image in the time series are arranged as a very large column vector of  $M$  brightness measurements. By discretizing the coronal volume in  $N$  cells, each LOS integral is expressed as a discrete sum of the known geometrical-scattering weighting factor evaluated at each computational cell threaded by the LOS times the unknown electron density in the respective cells. The column data vector of  $M$  intensities is then equal to a very large  $M \times N$  sparse projection matrix (containing only known factors depending on the observational geometry) multiplied by a column vector whose  $N$  elements are the unknown values of the coronal electron density in each cell of the computational grid. The non-square sparse projection matrix is not invertible. The linear inversion problem is then posed as a multidimensional optimization problem, in which there are  $N$  unknowns. The product of the projection matrix and the electron-density vector



represents the synthetic data. The solution of the problem is the one that best reproduces all images in the time series, as measured by the minimization functional, which is basically the squared norm of the difference between the observed and synthetic data.

Tomographic solutions are characterized by spurious high-spatial-frequency artifacts due to the poorly conditioned nature of the projection matrix (Frazin, Vásquez, and Kamalabadi, 2009). To mitigate this problem, inversion algorithms make use of regularization techniques (Frazin et al., 2007), which penalize non-physical large spatial gradients in the solution. This is implemented as an additional quadratic form in the minimization functional that approximates the spatial derivatives of the solution with a finite-difference approach (Frazin, Vásquez, and Kamalabadi, 2009). For detailed discussions on SRT, the reader is referred to the references provided here, and references therein.

While the VL detector of *Metis* has a size of  $2048^2$  pixels, the synoptic program is to be implemented with a lower resolution of  $512^2$ . This 16-fold binning, necessary to be able to continuously take images with a cadence of a few images per day, will also improve the signal-to-noise of the images. In the simulations of this work, the synthetic images were computed at this resolution.

To treat the tomographic problem, the coronal volume is discretized on a uniform spherical grid, with radial cell size  $\Delta r$ , and equal latitudinal  $\Delta\theta$  and azimuth cell size  $\Delta\phi$ . The specific radial and angular cell size were set in relation to the number of pixels in the images and the radial field of view of each case, as detailed next. The characteristic grid cell size described below is what is currently applied in a routine fashion in carrying out tomography based on data provided by the *Large Angle and Spectrometric CO*ronagraph (LASCO) C2 instrument, onboard the *Solar and Heliospheric Observatory* (SOHO), whose FoV covers heights comparable to those of *Metis* in its different orbital locations.

In the aphelion case, the full FoV linear size is  $L \approx 20.7R_{\odot}$ , with linear pixel size  $d \approx 0.04R_{\odot}$ . The tomographic cell size was set to  $\Delta r = 0.2R_{\odot}$  and  $\Delta\theta = 2^{\circ}$ . As the common radial FoV ranges  $5.7 - 10.3R_{\odot}$ , the average radial cell is located at height  $\langle r \rangle = 8.0R_{\odot}$ , with average angular linear size  $\langle \Delta l \rangle = \langle r \rangle \times \Delta\theta \approx 0.3R_{\odot}$ . In this way, the choice of grid size provides an average cell of linear dimensions  $\approx 0.2 \times 0.3R_{\odot}$ . Comparing that to the linear pixel size, note that such a cell in the plane-of-the-sky is threaded by  $\Delta r \times \langle \Delta l \rangle / d^2 \approx 38$  LOS. Every LOS is numerically treated individually, and then a 16-fold binning is applied, so that the average cell is threaded by two 16-binned LOS.

In the perihelion case, the full FoV linear size changes, with an average size  $\langle L \rangle \approx 7.3R_{\odot}$  and a linear pixel size  $d \approx 0.014R_{\odot}$ . The tomographic cell size was set to  $\Delta r = 0.1R_{\odot}$  and  $\Delta\theta = 2^{\circ}$ . As in this case, the common radial FoV ranges  $2.3 - 3.2R_{\odot}$ , the average radial cell is located at height  $\langle r \rangle = 2.75R_{\odot}$ , and its angular linear size then  $\langle \Delta l \rangle \approx 0.1R_{\odot}$ . In the plane-of-the-sky, such a cell is threaded by  $\approx 51$  LOS. Again, a 16-fold binning is applied, so that the average cell is effectively threaded by three 16-binned LOS.

In the maximum-latitude case, the full FoV linear size also changes, with an average size  $\langle L \rangle \approx 11.4R_{\odot}$ , and a linear pixel size  $d \approx 0.022R_{\odot}$ . The tomographic cell size was set to  $\Delta r = 0.1R_{\odot}$  and  $\Delta\theta = 2^{\circ}$ . As in this case, the common radial FoV ranges  $3.5 - 5.0R_{\odot}$ , the average radial cell is located at height  $\langle r \rangle = 4.25R_{\odot}$ , and its angular linear size then  $\langle \Delta l \rangle \approx 0.15R_{\odot}$ . In the plane-of-the-sky, such a cell is threaded by  $\approx 31$  LOS. Again, a 16-fold binning is applied, so that the average cell is effectively threaded by two 16-binned LOS.

### 3. Results

Tomographic reconstruction of the electron density of the two AWSoM simulations was implemented based on the image series synthesized around each of the three selected orbital segments, for a total of six reconstructions. In carrying out each reconstruction, two different values of the longitudinal step between consecutive observations were used:  $\Delta\phi = 12^\circ$  and  $6^\circ$ . The larger value was found to be optimal for the solar-minimum corona experiments, while the smaller one is optimal for the solar-maximum experiments. Results of the six reconstructions are reported next; each case using the optimal longitude step.

#### 3.1. Tomographic Reconstruction from Aphelion

For this orbital segment, tomographic reconstruction of the two AWSoM simulations was carried out over the radial FoV  $\approx 5.7 - 10.3 R_\odot$  common to all images in the series (Figure 2, top-left panel). Results for the solar-minimum and maximum simulations are shown in Figures 6 and 7, respectively. In both figures (from top to bottom), the first row of panels shows latitude–longitude maps of the electron density of the corresponding AWSoM model at heliocentric heights  $5.8 R_\odot$  (left panel) and  $10.2 R_\odot$  (right panel), near the lowest and largest height covered by the data. The second row of panels shows the corresponding maps of the tomographically reconstructed electron density. The third row of panels shows maps of the ratio between the electron density of the tomographic reconstruction and that of the model. The bottom-left panel shows the frequency histogram of the reconstruction-to-model electron-density ratio, for the whole reconstructed coronal volume.

For the two simulations, the histogram exhibits a median value  $\approx 1$ , with standard deviation  $\approx 12\%$  and  $\approx 22\%$  for the solar-minimum and solar-maximum models, respectively. The larger deviation in the case of the more complex corona is expected due to the richer small-scale structure, whose reconstruction is compromised by the regularization scheme. The bottom-right panel shows the global-average radial trend of the electron density, which is well reproduced by the tomographic reconstruction of both simulations.

#### 3.2. Tomographic Reconstruction from Perihelion

For this orbital segment, tomographic reconstruction of the two AWSoM simulations was carried out over the radial FoV  $\approx 2.3 - 3.2 R_\odot$  common to all images in the series (Figure 2, middle-left panel), although all the available data were used in constraining the inversion problem (including pixels outside the common FoV). Results for the solar-minimum and solar-maximum simulations are shown in Figures 8 and 9, respectively. In both figures, results are shown at heliocentric heights  $2.45 R_\odot$  and  $3.15 R_\odot$ , near (and within) the lowest and largest height of the reconstructed range of heights. Being based again on observations simulated from low latitudes, the accuracy of the tomographic reconstruction for the perihelion segment is comparable to the aphelion case. For both models, the global histogram of the reconstruction-to-model electron-density ratio again exhibits a median value  $\approx 1$ , with standard deviation  $\approx 14\%$  and  $\approx 22\%$  for the solar-minimum and solar-maximum models, respectively. The global-average radial trend of the electron density is again well reproduced by the tomographic reconstruction of both simulations.

#### 3.3. Tomographic Reconstruction from Maximum Solar Latitude

For this orbital segment, tomographic reconstruction of the two AWSoM simulations was carried out over the radial FoV  $\approx 3.5 - 5.0 R_\odot$  common to all images in the series (Figure 2,

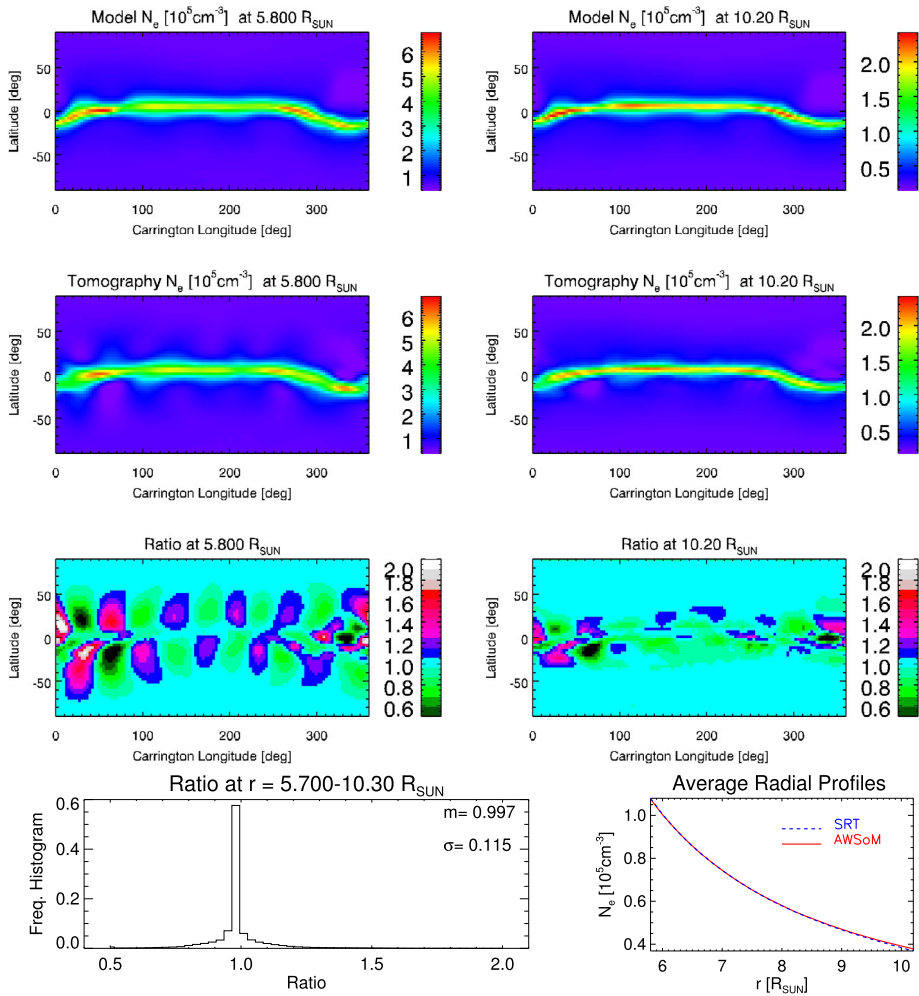


**Figure 6** Comparison of the CR 2082 solar-minimum simulation and its tomographic reconstruction for the aphelion segment. Maps are shown at heights  $5.8R_{\odot}$  (left panels) and  $10.2R_{\odot}$  (right panels). *Top panels*: latitude–longitude maps of the electron density [ $N_e$ ] of the model. *Second row of panels*: maps of  $N_e$  given by the tomographic reconstruction. *Third row of panels*: maps of the ratio between  $N_e$  of the tomographic reconstruction and of the model. *Bottom-left panel*: frequency histogram of the reconstruction-to-model electron-density ratio for the full reconstructed volume. The median [ $m$ ] and standard deviation [ $\sigma$ ] are indicated. *Bottom-right panel*:  $N_e(r)$  averaged over all latitudes and longitudes for the model (solid-red) and the reconstruction (dashed-blue).

bottom-left panel), although all the available data were used (as in the case of the perihelion segment). Results for the solar-minimum and solar-maximum simulations are shown in Figures 10 and 11, respectively. In both figures, results are shown at heliocentric heights  $3.55R_{\odot}$  and  $4.95R_{\odot}$ , near (and within) the lowest and largest height of the reconstructed range of heights.

Based on observations simulated from a (nearly constant) high latitude  $\theta \approx +32^\circ$ , the accuracy of the tomographic reconstruction for the solar-maximum-latitude segment is com-

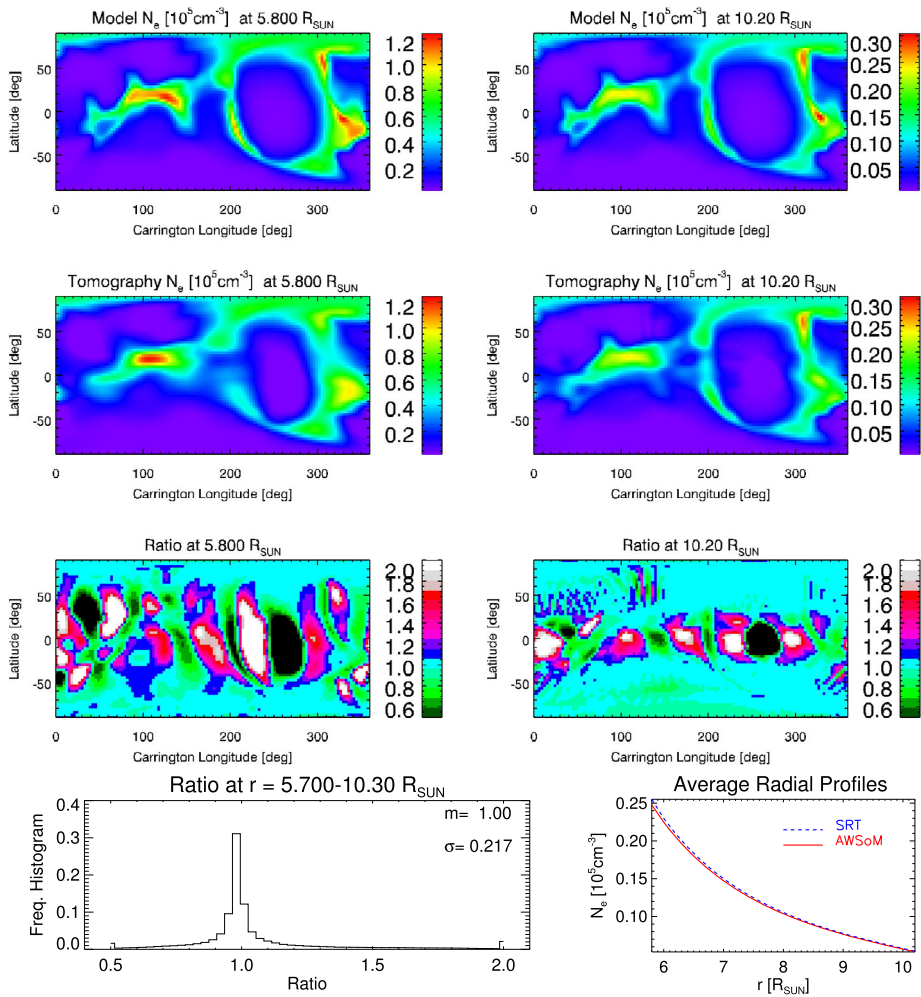


**Figure 7** Comparison of the CR 2152 solar-maximum simulation and its tomographic reconstruction for the aphelion segment. Maps are shown at heights  $5.8 R_{\odot}$  (left panels) and  $10.2 R_{\odot}$  (right panels). *Top panels:* latitude-longitude maps of the electron density  $[N_e]$  of the model. *Second row of panels:* maps of  $N_e$  given by the tomographic reconstruction. *Third row of panels:* maps of the ratio between  $N_e$  of the tomographic reconstruction and of the model. *Bottom-left panel:* frequency histogram of the reconstruction-to-model electron-density ratio for the full reconstructed volume. The median  $[m]$  and standard deviation  $[\sigma]$  are indicated. *Bottom-right panel:*  $N_e(r)$  averaged over all latitudes and longitudes for the model (solid-red) and the reconstruction (dashed-blue).

paratively less accurate than for both the aphelion and perihelion cases. Note how in the case of the solar-maximum simulation, the reconstruction fails for the range of latitudes  $\approx -90^\circ$  to  $\approx -50^\circ$ , a region largely non-accessed by the LOS of the observational sequence, due to the high (positive) latitude location of the spacecraft. Indeed, observing from a (nearly) constant latitude  $+\theta$  implies that coronal locations with latitude in the range  $[-90^\circ, -90^\circ + \theta]$  are not accessed by any LOS at low heights. Interestingly, the reconstruc-

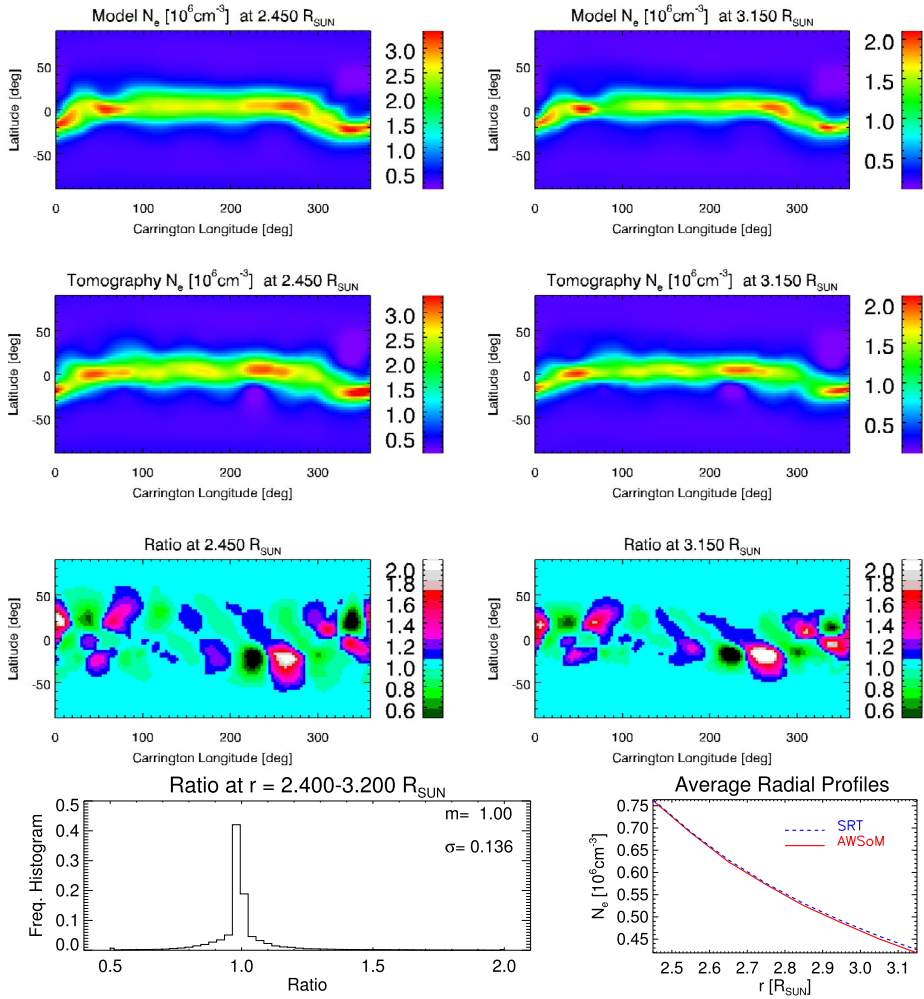


**Figure 8** Comparison of the CR 2082 solar-minimum simulation and its tomographic reconstruction for the perihelion segment. Maps are shown at heights  $2.45 R_{\odot}$  (left panels) and  $3.15 R_{\odot}$  (right panels). *Top panels*: latitude–longitude maps of the electron density [ $N_e$ ] of the model. *Second row of panels*: maps of  $N_e$  given by the tomographic reconstruction. *Third row of panels*: maps of the ratio between  $N_e$  of the tomographic reconstruction and of the model. *Bottom-left panel*: frequency histogram of the reconstruction-to-model electron-density ratio for the full reconstructed volume. The median [ $m$ ] and standard deviation [ $\sigma$ ] are indicated. *Bottom-right panel*:  $N_e(r)$  averaged over all latitudes and longitudes for the model (solid-red) and the reconstruction (dashed-blue).

tion of the solar-minimum simulation is not particularly inaccurate over that same latitude range. This is due to a combination of the corona being much simpler (in particular lacking small-scale structure at high latitudes) and the spatial regularization scheme of the tomography.

The global histogram of the reconstruction-to-model electron-density ratio exhibits a median value  $\approx 1.01$  for the solar-minimum simulation and  $\approx 1.05$  for the solar-maximum simulation. Also, for each simulation the standard deviation of the ratio histogram is the largest

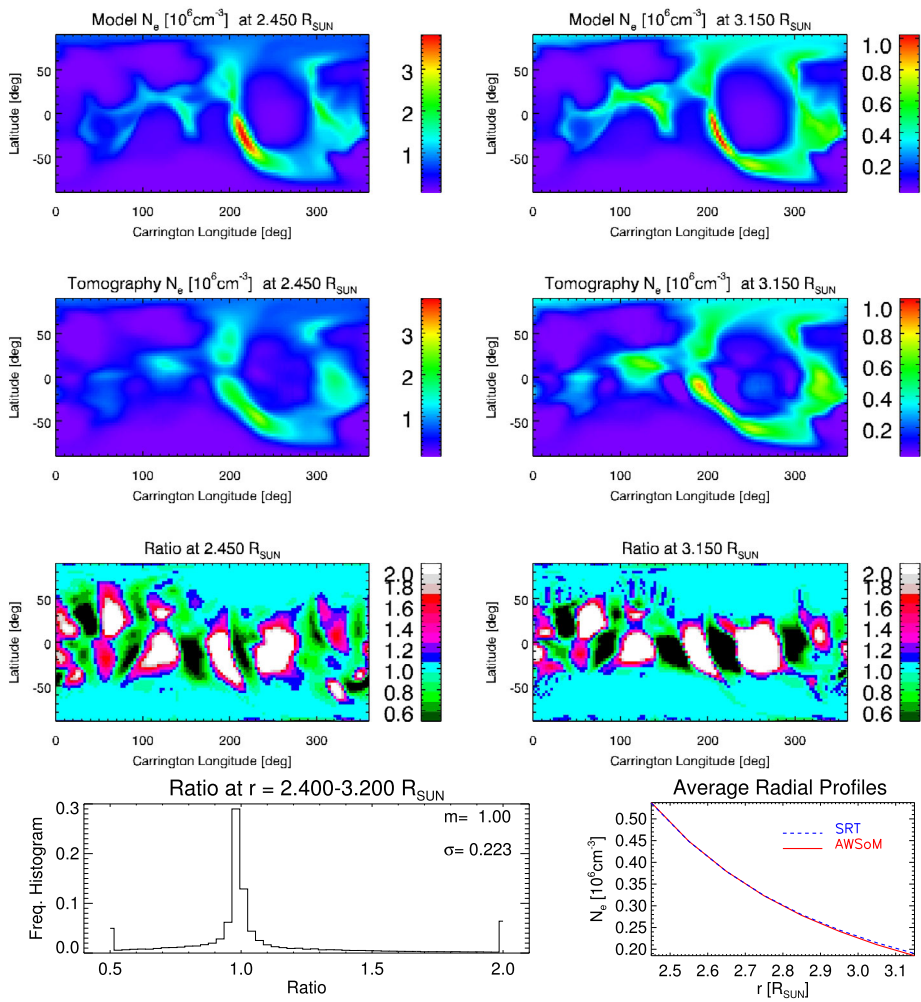


**Figure 9** Comparison of the CR 2152 solar-maximum simulation and its tomographic reconstruction for the perihelion segment. Maps are shown at heights  $2.45 R_{\odot}$  (left panels) and  $3.15 R_{\odot}$  (right panels). *Top panels*: latitude–longitude maps of the electron density [ $N_e$ ] of the model. *Second row of panels*: maps of  $N_e$  given by the tomographic reconstruction. *Third row of panels*: maps of the ratio between  $N_e$  of the tomographic reconstruction and of the model. *Bottom-left panel*: frequency histogram of the reconstruction-to-model electron-density ratio for the full reconstructed volume. The median [ $m$ ] and standard deviation [ $\sigma$ ] are indicated. *Bottom-right panel*:  $N_e(r)$  averaged over all latitudes and longitudes for the model (solid-red) and the reconstruction (dashed-blue).

of the values for the three orbital segments, being  $\approx 21\%$  and  $\approx 28\%$  for the solar-minimum and solar-maximum simulations, respectively. Likewise, the global average radial trend of the electron density departs from the model in a noticeable fashion (unlike in the aphelion and perihelion segments), with the difference being larger in the case of the solar-maximum simulation.

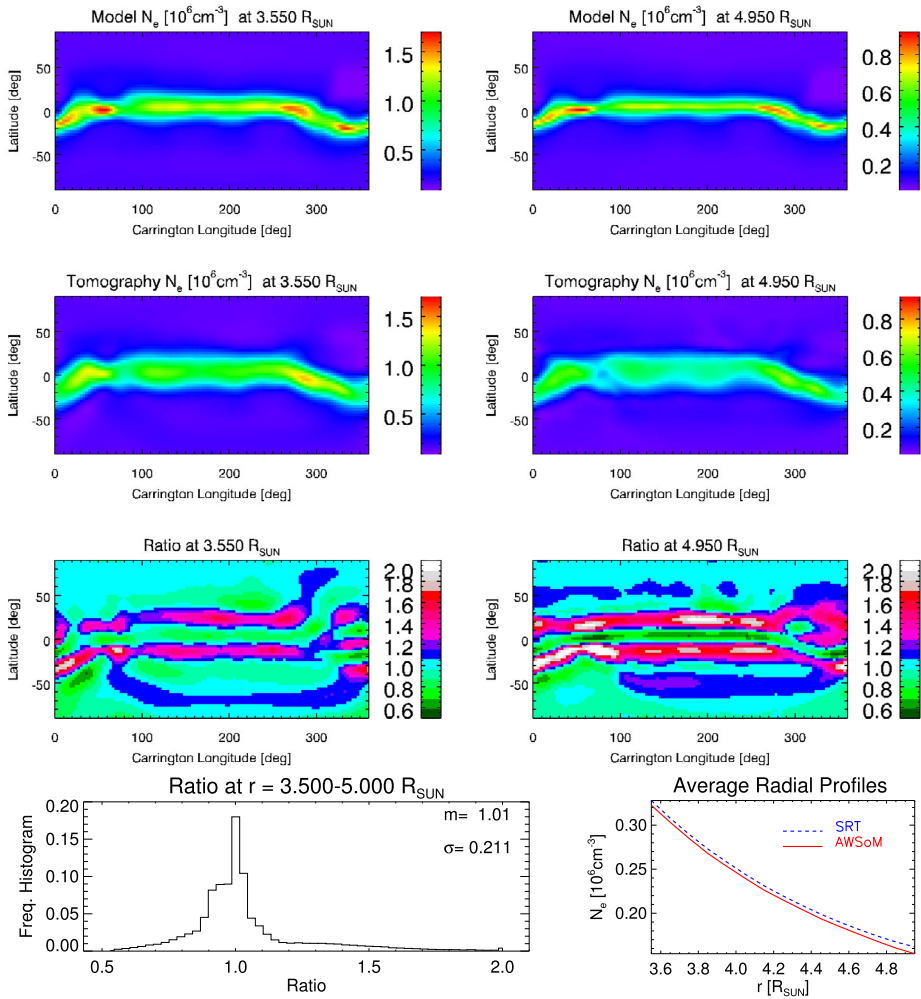


**Figure 10** Comparison of the CR 2082 solar-minimum simulation and its tomographic reconstruction for the maximum-latitude segment. Maps are shown at heights  $3.55 R_{\odot}$  (left panels) and  $4.95 R_{\odot}$  (right panels). *Top panels:* latitude–longitude maps of the electron density [ $N_e$ ] of the model. *Second row of panels:* maps of  $N_e$  given by the tomographic reconstruction. *Third row of panels:* maps of the ratio between  $N_e$  of the tomographic reconstruction and of the model. *Bottom-left panel:* frequency histogram of the reconstruction-to-model electron-density ratio for the full reconstructed volume. The median [ $m$ ] and standard deviation [ $\sigma$ ] are indicated. *Bottom-right panel:*  $N_e(r)$  averaged over all latitudes and longitudes for the model (solid-red) and the reconstruction (dashed-blue).

## 4. Conclusions and Discussion

This work explored the use of  $pB$ -images taken by a continuous synoptic program of observations by *Metis* to carry out tomographic reconstructions of the 3D distribution of the electron density of the solar corona. Based on steady-state 3D-MHD simulations of the solar corona and the orbital information of *Solar Orbiter*, time series of *Metis*  $pB$ -images were synthesized and used for tomographic reconstruction of the electron density of the model. Images were synthesized from three selected locations along the *Solar Orbiter* orbit: aphe-

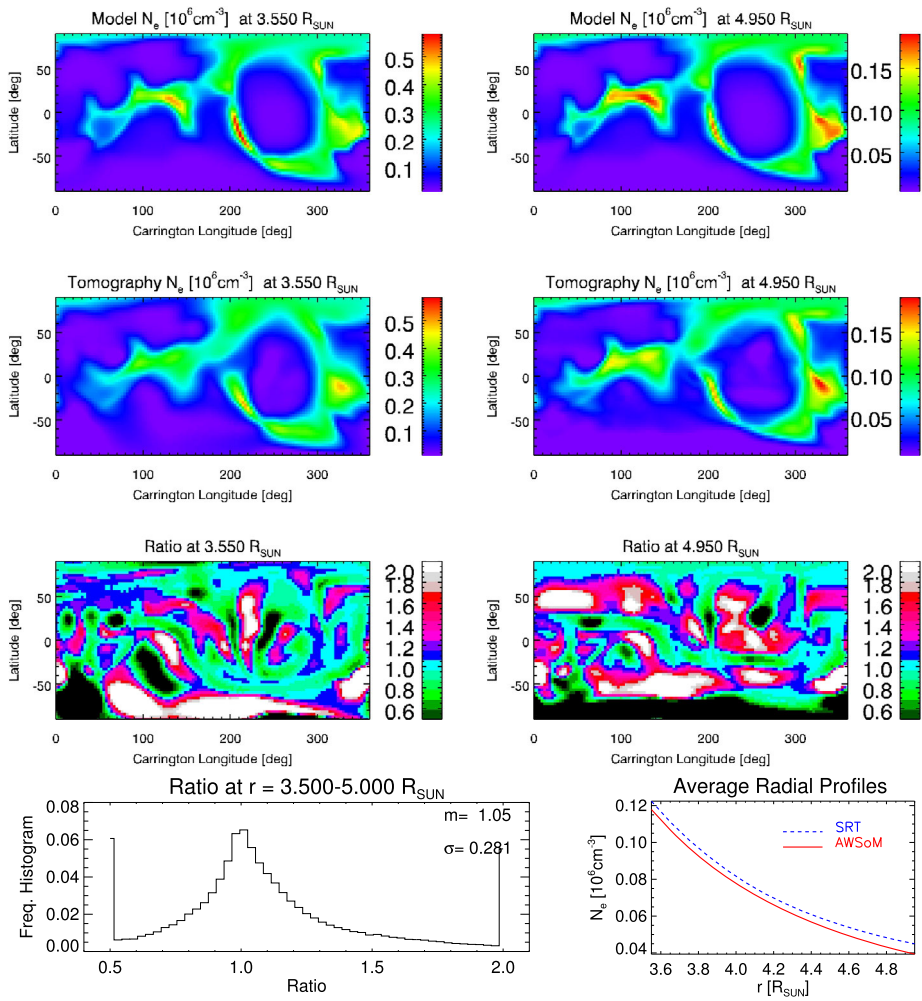


**Figure 11** Comparison of the CR 2152 solar-maximum simulation and its tomographic reconstruction for the maximum-latitude segment. Maps are shown at heights  $3.55 R_{\odot}$  (left panels) and  $4.95 R_{\odot}$  (right panels). *Top panels:* latitude–longitude maps of the electron density [ $N_e$ ] of the model. *Second row of panels:* maps of  $N_e$  given by the tomographic reconstruction. *Third row of panels:* maps of the ratio between  $N_e$  of the tomographic reconstruction and of the model. *Bottom-left panel:* frequency histogram of the reconstruction-to-model electron-density ratio for the full reconstructed volume. The median [ $m$ ] and standard deviation [ $\sigma$ ] are indicated. *Bottom-right panel:*  $N_e(r)$  averaged over all latitudes and longitudes for the model (solid-red) and the reconstruction (dashed-blue).

lion, perihelion, and maximum solar latitude, representing extreme geometrical conditions of observation by *Metis*. To experiment with both simple and complex coronal structure, three image sequences were synthesized based on two simulations of the solar corona, corresponding to a solar-minimum and a solar-maximum rotation. The main conclusions of this study are:

- Aphelion segment: the image sequence is obtained over a period of  $\approx 13$  days, and the range of heights over which the electron density can be reconstructed is  $\approx 5.7 - 10.3 R_{\odot}$ .



- Perihelion segment: the image sequence is obtained over a period of  $\approx 22$  days, and the range of heights over which the electron density can be reconstructed is  $\approx 2.3 - 3.2 R_{\odot}$ .
- For orbital segments in between aphelion and perihelion, the data-gathering period and the range of heights over which the density can be reconstructed are intermediate to the results presented above (see next point as an example).
- Maximum-solar-latitude segment: the image sequence is obtained over a period of  $\approx 16$  days, and the range of heights over which the electron density can be reconstructed is  $\approx 3.5 - 5.0 R_{\odot}$ .
- Observing from low-solar-latitude locations, such as the aphelion and perihelion segments explored in this work, the tomographic reconstruction is highly successful for both the solar-minimum and -maximum simulations.
- Observing from larger solar-latitude locations, such as the maximum solar-latitude segment explored in this work, tomographic reconstruction is not feasible over the high latitudes of the hemisphere opposite to the location of *Solar Orbiter*. Even so, a large fraction of the coronal volume can be satisfactorily reconstructed in this case.
- In the case of a simple dipolar corona, tomographic reconstructions required consecutive images taken from locations separated by a solar-longitude step  $\Delta\phi = 12^{\circ}$ . In the case of a highly complex corona, the solar-longitude step was reduced to  $\Delta\phi = 6^{\circ}$  to achieve satisfactory results.
- The observational cadence in these simulations ranges from  $\approx 0.7$  images  $\text{day}^{-1}$  (perihelion segment) to  $\approx 1.2$  images  $\text{day}^{-1}$  (aphelion segment), for the solar-minimum experiment. In the case of the solar-maximum experiment, the optimal cadence values are twice as large, ranging  $\approx 1.4 - 2.4$  images  $\text{day}^{-1}$ .

The cadence values found in this study to be optimal for tomography with *Metis* can be approximately replicated at any point of the *Solar Orbiter* orbit with a synoptic program providing at least four images  $\text{day}^{-1}$ . This is well within the capability of the current *Metis* synoptic program, performing synoptic observations with a two- to three-hour cadence, allowing for experimentation with other cadence values as well. This current program will also provide data redundancy (useful for validation of tomographic reconstructions). Its cadence will also provide a continuous opportunity to select images avoiding highly dynamic events, which compromise the accuracy of tomographic reconstructions.

This study was based on steady-state simulations, so that the reconstructions were not affected by dynamics-induced artifacts. In dealing with actual *Metis* data, the optimal observational cadence for a specific period of interest will also depend on the observed level of coronal dynamics, and various cadence values will be tried. Previous experience implementing tomography with LASCO-C2 data indicates that one image  $\text{day}^{-1}$  (implying  $\Delta\phi \approx 13^{\circ}$  for LASCO-C2) is around optimal (P. Lamy, private communication, 2021). In the case of actual data, the perihelion case will likely be more difficult to tackle than the aphelion case, because the data-acquisition time is longer and the corona is more highly structured at lower heights.

The varying degree of dynamical evolution exhibited by the solar corona during the 13–22 day data-acquisition period required for tomography with *Metis* at different segments along the orbit of *Solar Orbiter* will introduce artifacts in the reconstructions in the form of unreconstructed regions dubbed “zero-density artifacts” (ZDAs: Frazin, 2000; Frazin and Janzen, 2002). These can be mitigated using time-dependent tomographic-reconstruction schemes and also by partial masking of the images (Butala et al., 2010; Vibert et al., 2016). Different approaches will be investigated with actual images in order to assess how dynamics-induced artifacts can be best handled in the case of *Metis* observations.

Another approach to mitigate ZDAs in reconstructions of the solar corona that has not been explored so far is the approach of neural-network algorithms. Training such a neural network will require constructing a large data base of simulated data pairs of known temporally evolving models (with varying degrees of dynamics) and their reconstructions based on synthetic images. This novel approach will be explored in the future for tomography with VL instruments, such as *Metis* and LASCO-C2, as well as for EUV tomography.

Besides the specific solar-physics interest of tomographic reconstructions of the solar corona in general, there is also a side technical benefit from implementing reconstructions with data provided by *Metis* at any suitable opportunity. Along most of the *Solar Orbiter* orbit, the radial FoV of *Metis* overlaps with that of preexisting and still operating space-borne VL coronagraphs, such as SOHO/LASCO-C2 and *Solar Terrestrial Relations Observatory-A/COR1-2* (Frazin et al., 2012). Despite their different observational view angles, a statistical comparison of the results of independent and simultaneous tomographic reconstructions of the coronal electron density based on images from different instruments can be used as an intercalibration tool among them.

As a closing comment, we plan to combine VL tomography with tomography based on *Metis* H I Lyman- $\alpha$  images. This will in principle allow 3D mapping of the Lyman- $\alpha$  Doppler-dimming factor. Those results could then be inverted to compute 3D maps of the solar-wind velocity (Bemporad et al., 2021; Romoli et al., 2021). This project will be the focus of a subsequent effort.

**Acknowledgments** The authors acknowledge the thorough revision of the anonymous reviewers, which led to significant improvement of the article both in terms of richness of content and clarity of exposition.

*Solar Orbiter* is a space mission of international collaboration between ESA and NASA, operated by ESA. *Metis* was built and operated with funding from the Italian Space Agency (ASI), under contracts to the National Institute of Astrophysics (INAF) and industrial partners. *Metis* was built with hardware contributions from Germany (Bundesministerium für Wirtschaft und Energie through DLR), from the Czech Republic (PRODEX), and from ESA.

This work utilizes data obtained by the *Global Oscillation Network Group* (GONG) program, managed by the National Solar Observatory, which is operated by AURA, Inc. under a cooperative agreement with the National Science Foundation. The data were acquired by instruments operated by the Big Bear Observatory, High Altitude Observatory, Learmonth Solar Observatory, Udaipur Solar Observatory, Instituto de Astrofísica de Canarias, and Cerro Tololo Interamerican Observatory.

**Funding** A.M. Vásquez and F.A. Nuevo were partially supported by ANPCyT grant PICT-2016/0221 and CONICET grant PIP-11220200101169 to IAFE. F. Frassati is supported through the *Metis* program funded by the Italian Space Agency (ASI) under the contracts to the cofinancing National Institute of Astrophysics (INAF): Accordo ASI-INAF No. 2018-30-HH.0. N. Sachdeva and W.B. Manchester IV were supported by the NSF PRE-EVENTS grant No. 1663800 and the NSF SWQU grant No. PHY-2027555. High-performance computing support for these simulations was provided by Frontera (DOI) sponsored by NSF and the NASA supercomputing system Pleiades.

**Materials Availability** The 3D electron-density of the AWSoM simulations, their tomographic reconstructions, their computational grid, an IDL script to read those products into memory, and the synthetic images used for tomography, can be downloaded from the following repository: [doi.org/10.5281/zenodo.6916541](https://doi.org/10.5281/zenodo.6916541).

## Declarations

**Conflict of Interest** The authors declare that they have no conflicts of interest.

## References

- Antonucci, E., Romoli, M., Andretta, V., Fineschi, S., Heinzel, P., Moses, J.D., Naletto, G., Nicolini, G., Spadaro, D., Teriaca, L., Berlicki, A., Capobianco, G., Crescenzo, G., Da Deppo, V., Focardi, M., Frassetto, F., Heerlein, K., Landini, F., Magli, E., Marco Malvezzi, A., Massone, G., Melich, R., Nicolosi, P.,





- Noci, G., Pancrazzi, M., Pelizzo, M.G., Poletto, L., Sasso, C., Schühle, U., Solanki, S.K., Strachan, L., Susino, R., Tondello, G., Uslenghi, M., Woch, J., Abbo, L., Bemporad, A., Casti, M., Dolei, S., Grimani, C., Messerotti, M., Ricci, M., Straus, T., Telloni, D., Zuppella, P., Auchère, F., Bruno, R., Ciaravella, A., Corso, A.J., Alvarez Copano, M., Aznar Cuadrado, R., D'Amicis, R., Enge, R., Gravina, A., Jejičić, S., Lamy, P., Lanzafame, A., Meierdierks, T., Papagiannaki, I., Peter, H., Fernandez Rico, G., Giday Sertsu, M., Staub, J., Tsinganos, K., Velli, M., Ventura, R., Verroi, E., Vial, J.-C., Vives, S., Volpicelli, A., Werner, S., Zerr, A., Negri, B., Castronuovo, M., Gabrielli, A., Bertacin, R., Carpentiero, R., Natalucci, S., Marliani, F., Cesa, M., Laget, P., Morea, D., Pieraccini, S., Radaelli, P., Sandri, P., Sarra, P., Cesare, S., Del Forno, F., Massa, E., Montabone, M., Mottini, S., Quattropiani, D., Schillaci, T., Boccardo, R., Brando, R., Pandi, A., Baietto, C., Bertone, R., Alvarez-Herrero, A., García Pajejo, P., Cebollero, M., Amoruso, M., Centonze, V.: 2020, *Metis*: the Solar Orbiter visible light and ultraviolet coronal imager. *Astron. Astrophys.* **642**, A10. DOI ADS.
- Arge, C.N., Henney, C.J., Hernandez, I.G., Toussaint, W.A., Koller, J., Godinez, H.C.: 2013, Modeling the corona and solar wind using ADAPT maps that include far-side observations. In: Zank, G.P., Borovsky, J., Bruno, R., Cirtain, J., Cranmer, S., Elliott, H., Giacalone, J., Gonzalez, W., Li, G., Marsch, E., Moebius, E., Pogorelov, N., Spann, J., Verkhoglyadova, O. (eds.) *SOLAR WIND 13: Proc. Thirteenth International Solar Wind Conference CP-1539*, AIP, Melville, 11. DOI ADS.
- Barbey, N., Guennou, C., Auchère, F.: 2013, TomograPy: a fast, instrument-independent, solar tomography software. *Solar Phys.* **283**, 227. DOI ADS.
- Bemporad, A., Giordano, S., Zangrilli, L., Frassati, F.: 2021, Combining white light and UV Lyman- $\alpha$  coronagraphic images to determine the solar wind speed. The quick inversion method. *Astron. Astrophys.* **654**, A58. DOI ADS.
- Butala, M.D., Hewett, R.J., Frazin, R.A., Kamalabadi, F.: 2010, Dynamic three-dimensional tomography of the Solar Corona. *Solar Phys.* **262**, 495. DOI ADS.
- Frazin, R.A.: 2000, Tomography of the Solar Corona. I. A robust, regularized, positive estimation method. *Astrophys. J.* **530**, 1026. DOI ADS.
- Frazin, R.A., Janzen, P.: 2002, Tomography of the Solar Corona. II. Robust, regularized, positive estimation of the three-dimensional electron density distribution from LASCO-C2 polarized white-light images. *Astrophys. J.* **570**, 408. DOI ADS.
- Frazin, R.A., Vásquez, A.M., Kamalabadi, F.: 2009, Quantitative, three-dimensional analysis of the global corona with multi-spacecraft differential emission measure tomography. *Astrophys. J.* **701**, 547. DOI ADS.
- Frazin, R.A., Vásquez, A.M., Kamalabadi, F., Park, H.: 2007, Three-dimensional tomographic analysis of a high-cadence LASCO-C2 polarized brightness sequence. *Astrophys. J. Lett.* **671**, L201. DOI ADS.
- Frazin, R.A., Vásquez, A.M., Thompson, W.T., Hewett, R.J., Lamy, P., Llebaria, A., Vourlidis, A., Burkepile, J.: 2012, Intercomparison of the LASCO-C2, SECCHI-COR1, SECCHI-COR2, and Mk4 coronagraphs. *Solar Phys.* **280**, 273. DOI ADS.
- García Marirrodiga, C., Pacros, A., Strandmoe, S., Arcioni, M., Arts, A., Ashcroft, C., Ayache, L., Bonnefous, Y., Brahimi, N., Cipriani, F., Damasio, C., De Jong, P., Déprez, G., Fahmy, S., Fels, R., Fiebrich, J., Hass, C., Hernández, C., Icardi, L., Junge, A., Kletzkine, P., Laget, P., Le Deuff, Y., Liebold, F., Lodioli, S., Marliani, F., Mascarello, M., Müller, D., Oganessian, A., Olivier, P., Palombo, E., Philippe, C., Ragnit, U., Ramachandran, J., Sánchez Pérez, J.M., Stienstra, M.M., Thürey, S., Urwin, A., Wirth, K., Zouganelis, I.: 2021, Solar Orbiter: mission and spacecraft design. *Astron. Astrophys.* **646**, A121. DOI ADS.
- Lloveras, D.G., Vásquez, A.M., Nuevo, F.A., Mac Cormack, C., Sachdeva, N., Manchester, W., Van der Holst, B., Frazin, R.A.: 2020, Thermodynamic structure of the Solar Corona: tomographic reconstructions and MHD modeling. *Solar Phys.* **295**, 76. DOI ADS.
- Minnaert, M.: 1930, On the continuous spectrum of the corona and its polarisation. With 3 figures. *Z. Astrophys.* **1**, 209. ADS.
- Müller, D., St. Cyr, O.C., Zouganelis, I., Gilbert, H.R., Marsden, R., Nieves-Chinchilla, T., Antonucci, E., Auchère, F., Berghmans, D., Horbury, T.S., Howard, R.A., Krucker, S., Maksimovic, M., Owen, C.J., Rochus, P., Rodriguez-Pacheco, J., Romoli, M., Solanki, S.K., Bruno, R., Carlsson, M., Fludra, A., Harra, L., Hassler, D.M., Livi, S., Louarn, P., Peter, H., Schühle, U., Teriaca, L., del Toro Iniesta, J.C., Wimmer-Schweingruber, R.F., Marsch, E., Velli, M., De Groof, A., Walsh, A., Williams, D.: 2020, The Solar Orbiter mission. Science overview. *Astron. Astrophys.* **642**, A1. DOI ADS.
- Romoli, M., Antonucci, E., Andretta, V., Capuano, G.E., Da Deppo, V., De Leo, Y., Downs, C., Fineschi, S., Heinzl, P., Landini, F., Liberatore, A., Naletto, G., Nicolini, G., Pancrazzi, M., Sasso, C., Spadaro, D., Susino, R., Telloni, D., Teriaca, L., Uslenghi, M., Wang, Y.M., Bemporad, A., Capobianco, G., Casti, M., Fabi, M., Frassati, F., Frassetto, F., Giordano, S., Grimani, C., Jerse, G., Magli, E., Massone, G., Messerotti, M., Moses, D., Pelizzo, M.G., Romano, P., Schühle, U., Slemmer, A., Stangalini, M., Straus, T., Volpicelli, C.A., Zangrilli, L., Zuppella, P., Abbo, L., Auchère, F., Aznar Cuadrado, R., Berlicki, A.,

- Bruno, R., Ciaravella, A., D'Amicis, R., Lamy, P., Lanzafame, A., Malvezzi, A.M., Nicolosi, P., Nisticò, G., Peter, H., Plainaki, C., Poletto, L., Reale, F., Solanki, S.K., Strachan, L., Tondello, G., Tsinganos, K., Velli, M., Ventura, R., Vial, J.C., Woch, J., Zimbardo, G.: 2021. First light observations of the solar wind in the outer corona with the Metis coronagraph. [arXiv](#). [ADS](#).
- Sachdeva, N., Tóth, G., Manchester, W.B., van der Holst, B., Huang, Z., Sokolov, I.V., Zhao, L., Shidi, Q.A., Chen, Y., Gombosi, T.I., Henney, C.J., Lloveras, D.G., Vásquez, A.M.: 2021. Simulating solar maximum conditions using the Alfvén wave Solar Atmosphere Model (AWSoM). *Astrophys. J.* **923**, 176. [DOI](#). [ADS](#).
- Sokolov, I.V., van der Holst, B., Oran, R., Downs, C., Roussev, I.I., Jin, M., Manchester, I., Ward, B., Evans, R.M., Gombosi, T.I.: 2013. Magnetohydrodynamic waves and coronal heating: unifying empirical and MHD turbulence models. *Astrophys. J.* **764**, 23. [DOI](#). [ADS](#).
- van de Hulst, H.C.: 1950, The electron density of the solar corona. *Bull. Astron. Inst. Neth.* **11**, 135. [ADS](#).
- van der Holst, B., Sokolov, I.V., Meng, X., Jin, M., Manchester, W.B. IV, Tóth, G., Gombosi, T.I.: 2014, Alfvén Wave Solar Model (AWSoM): coronal heating. *Astrophys. J.* **782**, 81. [DOI](#). [ADS](#).
- Vásquez, A.M.: 2016, Seeing the solar corona in three dimensions. *Adv. Space Res.* **57**, 1286. [DOI](#). [ADS](#).
- Vásquez, A.M., Frazin, R.A., Vourlidas, A., Manchester, W.B., van der Holst, B., Howard, R.A., Lamy, P.: 2019, Tomography of the Solar Corona with the wide-field imager for the Parker Solar Probe. *Solar Phys.* **294**, 81. [DOI](#). [ADS](#).
- Vibert, D., Peillon, C., Lamy, P., Frazin, R.A., Wojak, J.: 2016, Time-dependent tomographic reconstruction of the solar corona. *Astron. Comput.* **17**, 144. [DOI](#). [ADS](#).

**Publisher's Note** Springer Nature remains neutral with regard to jurisdictional claims in published maps and institutional affiliations.

Springer Nature or its licensor holds exclusive rights to this article under a publishing agreement with the author(s) or other rightsholder(s); author self-archiving of the accepted manuscript version of this article is solely governed by the terms of such publishing agreement and applicable law.

## Authors and Affiliations

Alberto M. Vásquez<sup>1,2</sup>  · Federico A. Nuevo<sup>1,3</sup>  · Federica Frassati<sup>4</sup>  ·  
Alessandro Bemporad<sup>4</sup>  · Richard A. Frazin<sup>5</sup>  · Marco Romoli<sup>6</sup>  ·  
Nishtha Sachdeva<sup>5</sup>  · Ward B. Manchester IV<sup>5</sup> 

✉ A.M. Vásquez  
[alberto.vasquez@conicet.gov.ar](mailto:alberto.vasquez@conicet.gov.ar)

F.A. Nuevo  
[federico.nuevo@conicet.gov.ar](mailto:federico.nuevo@conicet.gov.ar)

F. Frassati  
[federica.frassati@inaf.it](mailto:federica.frassati@inaf.it)

A. Bemporad  
[alessandro.bemporad@inaf.it](mailto:alessandro.bemporad@inaf.it)

R.A. Frazin  
[rfrazin@umich.edu](mailto:rfrazin@umich.edu)

M. Romoli  
[marco.romoli@unifi.it](mailto:marco.romoli@unifi.it)

N. Sachdeva  
[nishthas@umich.edu](mailto:nishthas@umich.edu)

W.B. Manchester IV  
[chipm@umich.edu](mailto:chipm@umich.edu)

<sup>1</sup> Instituto de Astronomía y Física del Espacio (IAFE), National Council for Scientific and Technological Research (CONICET) - University of Buenos Aires (UBA), Ciudad de Buenos Aires, Argentina

- <sup>2</sup> Universidad Nacional de Tres de Febrero (UNTREF), Departamento de Ciencia y Tecnología, Caseros, Prov. de Buenos Aires, Argentina
- <sup>3</sup> Universidad de Buenos Aires (UBA), Ciclo Básico Común (CBC), Ciudad de Buenos Aires, Argentina
- <sup>4</sup> Istituto Nazionale di Astrofisica (INAF), Osservatorio Astrofisico di Torino, Pino Torinese (To), Italy
- <sup>5</sup> Department of Climate and Space Sciences and Engineering (CLASP), University of Michigan, Ann Arbor, MI, USA
- <sup>6</sup> Dipartimento di Fisica e Astronomia, Università degli Studi di Firenze (UniFI), Firenze, Italy